Asociación Argentina
de Mecánica Computacional

Mecánica Computacional Vol XXXII, págs. 1519-1537 (artículo completo)
Carlos G. García Garino, Aníbal E. Mirasso, Mario A. Storti, Miguel E. Tornello (Eds.)
Mendoza, Argentina, 19-22 Noviembre 2013

SIMULATION OF A LIFTING SURFACE WITH A FLEXIBLE PIEZOELECTRIC ACTUATOR IN A ROTATING ENVIRONMENT

Nicolás G. Tripp[a,c], Sergio Preidikman[b,c], Anibal E. Mirasso[a]

[a]*IMERIS,Facultad de Ingeniería, Universidad Nacional de Cuyo, Parque General San Martín, 5501 Mendoza, Argentina, aemirasso@uncu.edu.ar*

[b]*Departamento de Estructuras, Facultad de C. E. F. y N., Universidad Nacional de Córdoba, Casilla de Correo 916, 5000 Córdoba, Argentina, spreidikman@efn.uncor.edu*

[c]*Conicet CCT Mendoza, ntripp@mendoza-conicet.gob.ar*

Keywords: Wind Energy, Smart Blades, Aeroservoelasticity, Piezoelectric transducers.

Abstract. In the past years, the consumption of energy produced by wind turbines had an exponential growth. This requirement gave momentum to the development of larger turbines with the goal of producing more energy at the same site, reducing the initial investment, and the operation and maintenance costs. In order to achieve this objective, longer, lighter, maintenance-free blades are required so that smaller loads are transferred to the other, more expensive, wind turbine components. The resulting larger flexibility, imposes new challenges to the blade and controller designs; henceforth, new concepts are being developed to add more intelligence into these systems. During the last few years, the electronics industry had invested resources into the research and development of practical applications for piezoelectric ceramic materials. The result of this effort was the development of high precision piezoelectric actuators and sensors, which achieve forces and deformations that are compatible with the ones needed for the control of aerodynamic surfaces.

In a former study made by the authors, the aeroservoelastic behavior of a lifting surface with a fixed end and a flexible piezoelectric actuator was analyzed. In that work it was shown that the flexible piezoelectric actuator is an effective tool for vibration control. In the present paper, the analysis of the aeroservoelastic behavior of a lifting surface with a flexible piezoelectric actuator is extended to a non-inertial coordinate system that spins around an inertial one. The actuator is composed of a flexible trailing edge with embedded piezoelectric layers that enables the active control of the local aerodynamic forces. Structurally, both the flexible surface and flap are modeled as continuous beams with fixed-free end conditions. The displacements are described by a series expansion of assumed modes. The system aerodynamics are modeled with an unsteady version of the vortex lattice method (UVLM). High Reynolds number flow is assumed, therefore viscous effects are confined at the boundary layers and the wake shed by the surface. Both surface and wake are idealized as vortex sheets which in turn are discretized with vortex rings. In order to capture the physical aspects from the fluid-structure-control interaction, the aerodynamic and structural numerical models are combined by means of a strong coupling technique. The system equations of motion are integrated iteratively in the time domain. Numerical experiments are performed on a 100m test blade. The results show the feasibility of utilizing this type of actuators in the control of large horizontal axis wind turbines.

1 INTRODUCTION

The consumption of renewable energy produced by wind turbines had an exponential growth during last years. The development of large wind turbines producing more energy at the same site reducing the initial investment, the operation and maintenance costs, is an engineering challenge. In order to achieve this objective, longer, lighter, maintenance-free blades are required so that smaller loads are transferred to the other wind turbine components. The resulting larger flexibility imposes new challenges to the blade and controller design. Therefore new concepts are being developed to obtain better systems. There are several studies regarding this subject, mostly of them applied to aircraft and wind turbines. A good review can be seen in Barlas and Kuik (2010). In their work they state that "...trailing edge flap control seems to be one of the most efficient of the proposed aerodynamic control surfaces..".

The modeling of a lifting surface with an active smart flexible flap is not a simple task. Nonlinearities arise due to unsteady aerodynamics, complex structural properties such as shear, tension and mass center offset; but also due to the Fluid Structure Interaction (FSI), as discussed by Felippa et al (2001), i.e. the aerodynamic pressure responds to the shape of the flexible surface which is in turn a function of the aerodynamic pressure. Finally, adding a flexible trailing edge, capable of modifying its own geometry by means of a piezoelectric effect, in a predictable and useful manner, reveals the full complexity of the problem.

An efficient way for considering the aerodynamic effects over deformable bodies is the unsteady vortex lattice method (UVLM) used by Preidikman (1999) and Gebhardt (2008) among others. The former used UVLM to study the fluid structure interaction in smart wings; the latter applied the method to large horizontal axis wind turbines (LHAWT).

Regarding piezoelectric actuators, there is much ongoing research focused on improving the performance of wings, helicopter blades and wind turbines. For a general review see Giurgiutiu (2000) and Niezrecki et al (2001). One of the most common actuator configurations is known as unimorph, where two active layers of piezoelectric material are bonded to the exterior faces of a passive material layer. This structure allows a smooth bending control surface that prevents flow detachment. Pinkerton et al (1997) experimented on a thin layer composite-unimorph ferroelectric driver and sensor (THUNDER) piezoelectric actuator designed by NASA. Buhl et al (2007) studied the use of a THUNDER actuator as a trailing edge flap control for a wind turbine blade. A study on the two dimensional aeroservoelastic behavior of a wind turbine blade typical section, equipped with a smart flap, driven by a THUNDER actuator, has been presented by the authors (Tripp et al. (2011)). The results show that adding a simple plunge velocity feedback control law in the piezoelectric layers can increase bending damping up to 73% for the two dimensional case.

In this work, the aeroservoelastic behavior of a three dimensional lifting surface equipped with an active smart flap is numerically simulated in the time domain. The nonlinear aerodynamic effects are modeled with the UVLM, and the structural behavior is analyzed by means of Lagrange equations. The structural degrees of freedom are reduced with the assumed modes method. The latter is widely used in the helicopter industry and in some of the most popular aeroelastic codes for wind turbines, such as FAST (2005). To capture the physical aspects from the control-fluid-structure interaction, the models are combined using a strong coupling technique. The equations of motion of the aeroservoelastic system are integrated numerically and interactively in the time domain.

The present work is organized as follows. Firstly the main theoretical concepts are introduced. Secondly the actuator and controller design procedures are exposed. Next the

analysis is focused on the response of a 100m wind turbine blade-flap system embedded in a rotating environment at different speeds and undergoing plunging motion. Finally, the results are presented and discussed.

2 AEROSERVOELASTIC MODEL

In this section the aeroservoelastic model is described. Since the purpose of the present model is to simulate the response of wind turbine blades, the simulated surface will be referred as *surface* or *blade*. First the coordinate systems are introduced, then the structural model for the surface and the flap are presented. Next the UVLM model is introduced along with the force translation into modal coordinates. Then the resulting coupled system of equations is shown. Finally the numerical FSI coupling technique is presented.

2.1 Reference systems and nomenclature:

To describe the surface motion, three reference systems are defined as shown in figure 1.

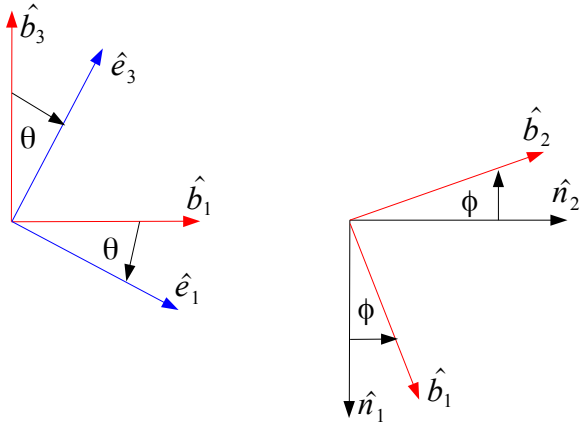

Figure 1: Reference systems.

The following definitions and conventions are used throughout this work:

$\hat{n}_1, \hat{n}_2, \hat{n}_3$: (*N*-system) Inertial system fixed in space.

$\hat{b}_1, \hat{b}_2, \hat{b}_3$: (*B*-system) Body system fixed to the body that rotates around the $\hat{n}_3$ axis.

$\hat{e}_1, \hat{e}_2, \hat{e}_3$: (*E*-system) Elastic system fixed to the local chord.

Small displacements and small deformations are assumed hence the *E*-system is rotated with the local elastic twist only.

$\phi(t)$: azimuthal angle defined around $\hat{n}_3$ axis.

β : pitch angle defined around $\hat{b}_2$ axis.

$\theta(y,t)$: elastic twist angle defined around $\hat{b}_2$ axis.

x, y, z : coordinates along the *B*-system.

x_e, y_e, z_e : coordinates along the *E*-system.

$h(y,t)$: is the out of plane displacement relative to the *B*-system.

$v(x,t)$: is the flap deflection relative to the *B*-system.

$d_1(y)$: is the distance offset of the section center of mass from the section shear center.

$\rho(y)$: is the section mass per unit length or *blade mass density*.

Bmass: is the blade total mass.

Lblade: is the blade total span.

TSR($\phi(t)$): is the tip speed ratio, which represents the ratio of the tangential speed of the tip of the blade over the free-stream speed.

The structural model comprises four degrees of freedom, namely the elastic out of plane displacement, the elastic twist angle, the azimuthal angle and the elastic flap deflection. Since the azimuthal angle represents a rigid body rotation, no stiffness is associated to this DOF. The section mass is lumped at the mass center and the section stiffness are lumped at the shear center. The line defined by all the mass centers is referred as *mass axis*, while the one defined by all the shear centers is the *elastic axis*. The time derivatives are noted with a dot superscript, while unit vectors are noted with a hat superscript. A bar superscript denotes a *pseudo-property*, i.e. $\bar{I}$ plays the role of a second moment of inertia though it is not strictly calculated as such.

2.2 Position and velocity vectors:

The position vector of point along the mass axis is shown as a red filled circle in figure 2. The undeformed blade is drawn in green dashed lines and the deformed blade in solid green lines. The dashed red line represents the mass axis, while the blue dashed line is the elastic axis.

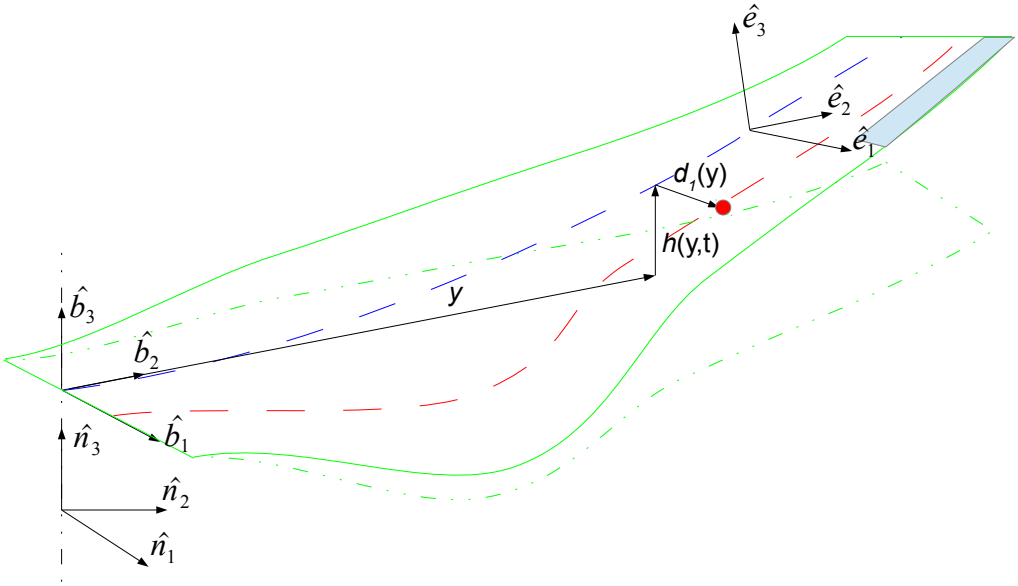

Figure 2: Position vector

Position of a point along the mass axis in the *R*-system:

$$\vec{r} = y\,\hat{b}_2 + h(y,t)\,\hat{b}_3 + x\,\hat{e}_1 = x\cos\theta(y,t)\,\hat{b}_1 + y\,\hat{b}_2 + [h(y,t) - x\sin\theta(y,t)]\,\hat{b}_3 \quad (1)$$

Only the fixed pitch case is considered.

Taking the time derivative of equation 1, and considering that the *B*-system is non inertial, i.e. taking the time derivative of the unit vectors thus exposing the azimuthal degree of freedom (see Meirovitch 1970), the velocity of the point in the *R*-system is found:

$$\begin{aligned} \vec{V}\cdot\hat{b}_1 &= [-\dot{\theta}(y,t)\,x\sin\theta(y,t) - \dot{\phi}(t)\,y\cos\beta] \\ \vec{V}\cdot\hat{b}_2 &= \phi(t)[x\cos(\theta(y,t)+\beta) + h(y,t)\sin\beta] \\ \vec{V}\cdot\hat{b}_3 &= [\dot{h}(y,t) - \dot{\theta}(y,t)\,x\cos\theta(y,t) - \dot{\phi}(y,t)\,y\sin\beta] \end{aligned} \quad (2)$$

2.3 Surface model:

To reduce the problem of continuous media with infinite degrees of freedom (DOF), the assumed modes method is used. The DOF are reduced to a finite number by means of two

series expansions, one for the out of plane displacement and the other for the torsion angle. In this work only the first term of the series is used:

$$\begin{aligned} h &= q_h(t)\varphi_h(y) \\ \theta &= q_\theta(t)\varphi_\theta(y) \end{aligned} \tag{3}$$

where $q_h(t)$ and $q_\theta(t)$ are time dependent generalized coordinates and $\varphi_h(y), \varphi_\theta(y)$ are space-dependent admissible functions (Meirovitch 1980), compatible with the boundary conditions. The system equations of motion for a discrete system can be obtained with the Lagrange equations:

$$\begin{aligned} &\frac{d}{dt}\left(\frac{\partial}{\partial \dot{q}_h}T\right)-\frac{\partial}{\partial q_h}T+\frac{\partial}{\partial q_h}U=Q_{qh} \\ &\frac{d}{dt}\left(\frac{\partial}{\partial \dot{q}_\theta}T\right)-\frac{\partial}{\partial q_\theta}T+\frac{\partial}{\partial q_\theta}U=Q_{q\theta} \\ &\frac{d}{dt}\left(\frac{\partial}{\partial \dot{\phi}}T\right)-\frac{\partial}{\partial \phi}T+\frac{\partial}{\partial \phi}U=Q_{\phi} \end{aligned} \tag{4}$$

where T is the kinetic energy, is the potential energy, and Q_h, Q_θ, Q_ϕ are the non-conservative generalized forces for the three DOF.

2.3.1 Kinetic energy:

The kinetic energy is defined as:

$$T(t)=\frac{1}{2}\int_0^{BMass}\vec{V}(t)\cdot\vec{V}(t)\,dm \tag{5}$$

Hence replacing (2) into (5):

$$T(t)=T_{hh}(t)+T_{\theta\theta}(t)+T_{\phi\phi}(t)+T_{h\theta}(t)+T_{h\phi}(t)+T_{\theta\phi}(t)$$

where

$$\begin{aligned} T_{hh}(t)&=\frac{1}{2}\dot{q}_h^2\int_0^{Lblade}\varphi_h^2(y)\rho(y)\,dy \\ T_{\theta\theta}(t)&=\frac{1}{2}\dot{q}_\theta^2\int_0^{Lblade}\varphi_\theta^2 d_1^2(y)\rho(y)\,dy \\ T_{\phi\phi}(t)&=\frac{1}{2}\dot{\phi}^2\left(\int_0^{Lblade}y^2\rho(y)\,dy+\int_0^{Lblade}(d_1(y)\cos(\theta(y,t)+\beta)+h(y,t)\sin\beta)^2\rho(y)\,dy\right) \\ T_{h\theta}(t)&=-\dot{q}_h\dot{q}_\theta\int_0^{Lblade}\varphi_h(y)\varphi_\theta(y)d_1(y)\cos(q_\theta\varphi_\theta)\rho(y)\,dy \\ T_{h\phi}(t)&=-\dot{q}_h\dot{\phi}\sin\beta\int_0^{Lblade}\varphi_h(y)\,y\rho(y)\,dy \\ T_{\theta\phi}(t)&=\dot{q}_\theta\dot{\phi}\int_0^{Lblade}\varphi_\theta(y)d_1(y)\,y\sin(\beta+\theta(y,t))\rho(y)\,dy \end{aligned} \tag{6}$$

2.3.2 Potential energy

The potential energy due to elastic bending and torsion is:

$$U(t)=\frac{1}{2}\int_0^{blade\,vol}\sigma_{yy}(y,z,t)\varepsilon_{yy}(y,z,t)\,dvol+\frac{1}{2}\int_0^{blade\,vol}\tau_{xz}(x,y,z,t)\gamma_{xz}(x,y,z,t)\,dvol \tag{7}$$

where:

$\sigma_{yy}(y,z,t)$ and $\varepsilon_{yy}(y,z,t)$ are the axial stress and strain of the beam.

$\tau_{xz}(x,y,z,t)$ and $\gamma_{xz}(x,y,z,t)$ are the torsional stress and angular distortion of the beam.

The stress and strain components are found considering Euler-Bernoulli beam theory hypotheses, uniform torsion and linear elastic material:

$$\begin{aligned}
&\varepsilon_{yy}(y,z,t)=-(z-z_n)\frac{\partial^2}{\partial y^2}h(y,t)\\
&\sigma_{yy}(y,z,t)=E\,\varepsilon_{yy}(y,z,t)\\
&\gamma_{xz}(x,y,z,t)=r(x,z)\frac{\partial}{\partial y}\theta(y,t)\\
&\tau_{xz}(x,y,z,t)=G\,\gamma_{xz}(x,y,z,t)
\end{aligned} \tag{8}$$

where:

z_n is the neutral axis location, is the radial distance from the shear center, E and G are the elastic isotropic young modulus and shear modulus.

Replacing the approximations for the elastic displacement and twist, i.e. replacing (3) into (8):

$$\begin{aligned}
&\varepsilon_{yy}(y,z,t)=-(z-z_n)q_h(t)\frac{\partial^2}{\partial y^2}\varphi_h(y)\\
&\gamma_{xz}(x,y,z,t)=r(x,z)q_\theta(t)\frac{\partial}{\partial y}\varphi_\theta(y)
\end{aligned} \tag{9}$$

Finally inserting (8) and (9) into (7) the potential energy equation is found:

$$U(t)=\frac{1}{2}q_h^2(t)\int_0^{Lblade}\left(\frac{\partial^2\varphi_h}{\partial y^2}\right)^2 EJ_{xx}(y)dy+\frac{1}{2}q_\theta^2(t)\int_0^{Lblade}\left(\frac{\partial\varphi_\theta}{\partial y}\right)^2 GJ_p(y)dy \tag{10}$$

where $EJ_{xx}(y)$ and $GJ_p(y)$ are the beam section bending stiffness and torsion stiffness.

Replacing (6) and (10) in (4) and grouping all the terms results in the following matrix form:

$$[M(t)]\begin{pmatrix}\ddot{q}_h(t)\\ \ddot{q}_\theta(t)\\ \ddot{\phi}(t)\end{pmatrix}+[K]\begin{pmatrix}q_h(t)\\ q_\theta(t)\\ \phi(t)\end{pmatrix}+[B(t)]\begin{pmatrix}\dot{q}_h(t)\\ \dot{q}_\theta(t)\\ \dot{\phi}(t)\end{pmatrix}=\begin{pmatrix}Q_h(t)\\ Q_\theta(t)\\ Q_\phi(t)\end{pmatrix} \tag{11}$$

where:

M is the mass matrix:

$$M(t)=\begin{bmatrix}m_{hh} & m_{h\theta} & m_{h\phi}\\ m_{\theta h} & m_{\theta\theta} & m_{\theta\phi}\\ m_{\phi h} & m_{\phi\theta} & m_{\phi\phi}\end{bmatrix}$$

$$m_{hh}=\int_0^{Lblade}\varphi_h^2(y)\rho(y)dy=\bar{m}$$

$$m_{h\theta}(t)=m_{\theta h}(t)=-\int_0^{Lblade}\varphi_h(y)\varphi_\theta(y)d_1(y)\cos\theta(y,t)\rho(y)dy=\bar{S}_y(t)$$

$$m_{h\phi}=m_{\phi h}=-\sin\beta\int_0^{Lblade}\varphi_h(y)y\rho(y)dy=\bar{S}_z$$

$$m_{\theta\theta}=\int_0^{Lblade}\varphi_\theta^2(y)d_1^2\rho(y)dy=\bar{I}_{yy}$$

$$m_{\theta\phi}(t)=m_{\phi\theta}(t)=\int_0^{Lblade}\varphi_\theta(y)d_1\,y\sin(\beta+\theta(y,t))\rho(y)dy=\bar{I}_{\theta\phi}(t)$$

$$m_{\phi\phi}(t)=\int_0^{Lblade}(y^2(y)+(d_1\cos(\theta(y,t)+\beta)+h(y,t)\sin\beta)^2)\rho(y)dy=I_{zz}(t)$$

K is the stiffness matrix:

$$K=\begin{bmatrix} k_{hh} & 0 & 0 \\ 0 & k_{\theta\theta} & 0 \\ 0 & 0 & k_{\phi\phi} \end{bmatrix}$$

$$k_{hh}=\int_0^{Lblade}\left(\frac{\partial^2}{\partial y^2}\varphi_h(y)\right)^2 EJ_{xx}(y)\,dy$$

$$k_{\theta\theta}=\int_0^{Lblade}\left(\frac{\partial}{\partial y}\varphi_\theta(y)\right)^2 GJ_p(y)\,dy$$

$$k_{\phi\phi}=0$$

And B is the gyroscopic matrix:

$$B(t)=\begin{bmatrix} 0 & \dot{q}_\theta(t)b_{h\theta}(t) & \dot{\phi}(t)b_{h\phi(t)} \\ 0 & 0 & \dot{\phi}(t)b_{\theta\phi}(t) \\ \dot{\phi}(t)b_{\phi h}(t) & \dot{q}_\theta(t)b_{\phi\theta}(t) & \dot{q}_\theta(t)b_{\phi\phi}(t) \end{bmatrix}$$

$$b_{h\theta}(t)=\int_0^{Lblade}\varphi_h(y)\varphi_\theta^2(y)d_1(y)\sin\theta(y,t)\rho(y)\,dy$$

$$b_{h\phi}(t)=-\sin\beta\int_0^{Lblade}\varphi_h(y)(d_1(y)\cos(\theta(y,t)+\beta)+h(y,t)\sin\beta)\rho(y)\,dy$$

$$b_{\theta\phi}(t)=\int_0^{Lblade}d_1(y)\sin(\theta(y,t)+\beta)\varphi_\theta(y)(d_1\cos(\theta(y,t)+\beta)+h(y,t)\sin\beta)\rho(y)\,dy$$

$$b_{\phi h}(t)=2\sin\beta\int_0^{Lblade}\varphi_h(y)(d_1(y)\cos(\theta(y,t)+\beta)+h(y,t)\sin\beta)\rho(y)\,dy$$

$$b_{\phi\theta}(t)=\int_0^{Lblade}\varphi_\theta^2(y)d_1(y)y\cos(\beta+\theta(y,t))\rho(y)\,dy$$

$$b_{\phi\phi}(t)=-2\int_0^{Lblade}d_1(y)\sin(\theta(y,t)+\beta)\varphi_\theta(y)(d_1(y)\cos(\theta(y,t)+\beta)+h(y,t)\sin\beta)\rho(y)\,dy$$

2.4 Flap model:

The flap mass is neglected against the blade total mass; it is modeled as an elastic surface, with fixed-free boundary conditions.

2.4.1 Piezoelectric material model:

For modeling the actuator, the *bender* reference architecture was used (Jalili 2010). The actuator is modeled as a beam made of a composite material, where the outer layers are made of piezoelectric PZT ceramic material and the inner layer is made of steel. The beam has fixed-free boundary conditions as shown in figure 3.

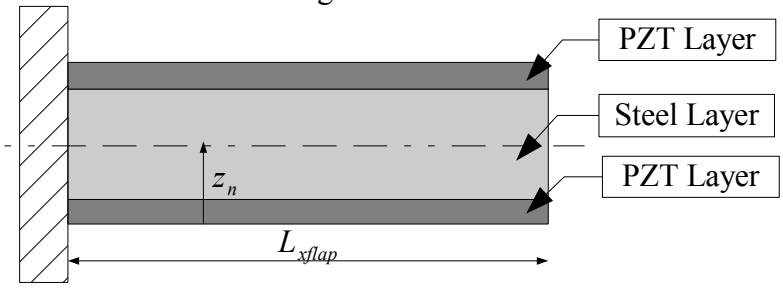

Figure 3: Flap Layout

The flap deflection, relative to the body of the blade, is described using the assumed modes method. As before only the first term of the expansion is used:

$$v(x_e,t)=q_{flap}(t)\varphi_{flap}(x_e)=q_{flap}(t)\left(\frac{x_e}{L_{xflap}}\right)^2 \tag{12}$$

where $q_{flap}(t)$ and $\varphi_{flap}(x)$ are the time-dependent generalized function and space-dependent admissible function respectively, x_e is the coordinate along the $\hat{e}_1$ axis and L_{xflap} is the flap length in the chord direction.

The flap strain energy is:

$$U_{flap}(t)=\int_0^{inner\,volume}\sigma_{xx}^{inner}(x_e,z_e,t)\varepsilon_{xx}(x_e,z_e,t)dvol+\int_0^{outer\,volume}\sigma_{xx}^{outer}(x_e,z_e,t)\varepsilon_{xx}(x_e,z_e,t)dvol \tag{13}$$

where $U_{flap}(t)$ is the potential energy, andare the axial stress components for the inner and outer layers respectively and $\varepsilon_{xx}(x_e,z_e,t)$ is the axial strain component.

The axial strain can be found considering Euler-Bernoulli beam theory hypotheses.

$$\varepsilon_{xx}(x_e,z_e,t)=-(z_e-z_n)\frac{\partial^2}{\partial x^2}v(x_e,t) \tag{14}$$

where once again z_n is the neutral axis location and $v(x,t)$ is the flap displacement.

The axial stress for the inner layer is found in the same way as in the blade calculations, while the axial stresses for the outer layers are found considering the direct piezoelectric effect:

$$\begin{aligned}\sigma_{xx}^{inner}(x_e,z_e,t)&=E\,\varepsilon_{xx}(x_e,z_e,t)\\ \sigma_{xx}^{outer}(x_e,z_e,t)&=c_{xx}^{\epsilon}[\varepsilon_{xx}(x_e,z_e,t)-d_{zx}\,\epsilon_{zz}]=c_{xx}^{\epsilon}[\varepsilon_{xx}(x_e,z_e,t)-d_{zx}\frac{V}{t_p}]\end{aligned} \tag{15}$$

where:

E: is the young modulus of the inner layer.

c_{xx}^{ϵ} : is the elastic young modulus of the outer layers under constant electric displacement.

$\varepsilon_{xx}(x_e,z_e,t)$: is the axial mechanical strain.

d_{zx} : is the electromechanical coupling coefficient.

ϵ_{zz} : is the electric field normal to the piezoelectric surface.

V : is the applied voltage.

t_p : is the piezoelectric layer thickness.

Replacing (12) into (14), the axial strain is defined in terms of the flap DOF:

$$\varepsilon_{xx}(x_e,z_e,t)=-q_{flap}(t)(z-z_n)\frac{2}{L_{xflap}^2} \tag{16}$$

The geometry of the flap is assumed uniform, hence replacing (15) and (16) into (13) and grouping terms results in:

$$U_{flap}(t)=\frac{4\,L_{yflap}(EI_{inner}+2\,EI_{outer})}{L_{xflap}^4}q_{flap}^2(t)+\frac{2\,L_{yflap}d_{zx}c_{xx}^{\epsilon}S_{outer}}{t_p\,L_{xflap}^2}\Delta V(t)q_{flap}(t) \tag{17}$$

where:

L_{yflap} : is the flap length in the span direction.

EI_{inner} : is the inner layer bending stiffness.

EI_{outer} : is the outer layer bending stiffness.

S_{outer} : is the outer layer first moment of inertia.

ΔV : is the difference between the voltage applied at the upper outer layer and the lower outer layer.

Since there is no flap kinetic energy, the Lagrange equation for the flap system reduces to a

static equilibrium equation:

$$\frac{\partial}{\partial q_{flap}} U_{flap}(t) = Q_{flap}(t) \tag{18}$$

where $Q_{flap}(t)$ is the non-conservative force due to the aerodynamic pressure over the flap. Replacing (17) into (18) we obtain the flap stiffness k_{flap} and the equivalent piezoelectric force F_{pzt}:

$$k_{flap} q_{flap}(t) + F_{pzt} V(t) = Q_{flap}(t)$$

where:

$$k_{flap} = \frac{8 L_{yflap} (EI_{inner} + 2 EI_{outer})}{L_{xflap}^4}$$

$$F_{pzt} = \frac{4 L_{yflap} d_{zx} c_{xx}^{\epsilon} S_{outer}}{t_p L_{xflap}^2} \tag{19}$$

2.5 Unsteady Vortex Lattice model:

This model follows the work of Preidikman (1998). The fluid is assumed to be incompressible and homogeneous. Forces are assumed irrotational. Since high Reynolds number flow is assumed, viscous effects are confined at the boundary layers and are shed into the wake at the trailing edge. No viscous diffusion takes place, hence the circulation around any closed material curve is invariant in time. Therefore the distribution of vorticity is idealized in terms of two vortex sheets (surface and wake) embedded in an irrotational domain. Both surface and wake vortex sheets are represented by a grid of discrete vortex rings as shown in figure 4. The no penetration condition is enforced at control points. The wake is allowed to move with the local velocity with a force-free condition. The vorticity of the rings in the wake sheet remains constant in time.

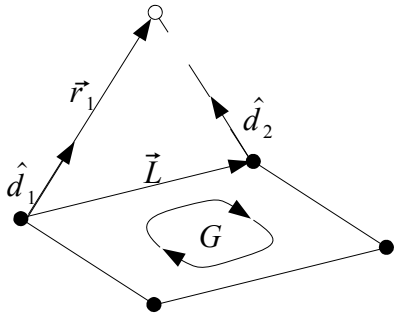

Figure 4: Vortex ring element

The velocity induced by a segment of the vortex ring at each control point is found from an integral representation, which for the case of a discrete ring can be written in the following vector form:

$$\vec{v}_i = G_j \sum_{k=1}^{4} \frac{1}{4\pi} \frac{\vec{L}_k \times \vec{r}_{1k}}{\left\| \vec{L}_k \times \vec{r}_{1k} \right\|_2^2} \left(\vec{L}_k \cdot (\hat{e}_{1k} - \hat{e}_{2k}) \right) = \vec{a}_{ij} G_j \tag{20}$$

where:

$\vec{v}_i$ is the induced velocity at the control point i.

G_j is the ring j strength.

$\hat{d}_{1k}, \hat{d}_{2k}$ are unit vectors pointing from the segment k endpoints to the control point.

$\vec{r}_{1k}$ is a vector defined by the first endpoint of the segment k and the control point i.
$\vec{L}_k$ is a vector defining the segment k length.
$\vec{a}_{ij}$ is the induced velocity of the vortex ring j with unit strength into the control point i.

The no penetration condition is enforced at each control point:

$$(\vec{v}_{surface}+\vec{v}_{wake}-\vec{v}_{\infty}-\vec{v}_{body})\cdot\hat{n}=0 \tag{21}$$

where:
$\vec{v}_{surface}$: is the velocity induced by the vortex sheet attached to the surface.
$\vec{v}_{wake}$: is the velocity induced by the wake vortex sheet shed from the surface.
$\vec{v}_{\infty}$: is the free stream velocity.
$\vec{v}_{body}$: is the velocity induced by the surface motion.
$\hat{n}$: is the surface normal unit vector.

Hence the evaluation of (21) at all the surface control points produces the following linear system of equations:

$$[A]\vec{G}=-(V_{wake}+V_{\infty}+V_{body})\cdot N \tag{22}$$

where:
$[A]$: is a matrix whose components are the induced velocities of all the surface vortex rings, with unit strength, at each control point.
G : is a vector containing the unknown surface vortex ring strengths.
$V_{wake}, V_{\infty}, V_{body}$: are matrices containing the velocities induced by the wake vortex sheet rings, the free stream and the surface motion, at each control point.
N : is a matrix containing the normal unit vector of every control point.

At each time step, the linear system of equations (22) is solved for the unknown vorticity G. The induced velocities at the surface and wake are then evaluated with (20) and the pressure jump at each element is determined using an unsteady version of the Bernoulli equation:

$$\Delta P=P_{dyn}\Delta Cp=P_{dyn}[2(\vec{V}_m-\vec{V}_{CP})\cdot\Delta\vec{V}+2\frac{D}{Dt}G_{CP}] \tag{23}$$

where:
ΔP is the pressure jump at a control point.
P_{dyn} is the free stream dynamic pressure.
ΔCp is the nondimensional pressure coefficient difference at each control point
$\vec{V}_m$ is the fluid tangential velocity nondimensionalized by the reference velocity.
$\vec{V}_{CP}$ is the surface velocity nondimensionalized by the reference velocity..
$\Delta\vec{V}$ is the tangential velocity jump across the sheet nondimensionalized by the reference velocity.
$\frac{D}{Dt}G_{CP}$ is the total derivative of the vortex ring strength.

Finally, time is advanced, the wake shape is updated using the local velocity field and all the previous calculation steps are repeated.

2.6 Generalized forces

The generalized non-conservative forces, which deform the elastic system, are retrieved from

the virtual work done by the aerodynamic pressure over the surface-flap system.

2.6.1 Blade forces

The virtual work produced by the aerodynamic pressure is the same as the one produced by the generalized non-conservative forces.

$$\delta \bar{W} = Q_{qh}(t)\delta q_h + Q_{q\theta}(t)\delta q_\theta + Q_\phi(t)\delta\phi = \int_0^{blade\ surface} \vec{df}(x,y,t)\cdot\delta\vec{r}(x,y,t) \tag{24}$$

where:

$\vec{f}(x,y,t)$: is the force produced by the aerodynamic pressure jump.

$\vec{r}(x,y,t)$: is the position vector (1).

The aerodynamic pressure jump is defined normal to the local chord:

$$\vec{df}(x,y,t) = \Delta p(x,y,t)\hat{e}_3 \tag{25}$$

Taking the variation of (1) and replacing it into (24), along with (25), and equating vector terms, the generalized non-conservative forces over the blade are found:

$$\begin{aligned} Q_{qh}(t) &= \int_0^{blade\ surface} \varphi_h(y)\cos\theta(y,t)\Delta p(x,y,t)\,dA \\ Q_{q\theta}(t) &= -\int_0^{blade\ surface} x\,\varphi_\theta(y)\Delta p(x,y,t)\,dA \\ Q_\phi(t) &= -\int_0^{blade\ surface} y\sin(\theta(y,t)+\beta)\Delta p(x,y,t)\,dA \end{aligned} \tag{26}$$

The pressure coefficient from (23) is defined as follows:

$$\Delta Cp = \frac{\Delta p}{\frac{1}{2}\rho_C V_C^2} \tag{27}$$

where ρ_C, V_C are the free-stream reference density and velocity respectively.

Hence replacing (27) into (26) the generalized forces can be rewritten:

$$\begin{aligned} Q_{qh}(t) &= \frac{1}{2}\rho_{air}V_\infty^2\int_0^{blade\ surface} \varphi_h(y)\cos\theta(y,t)Cp(x,y,t)\,dA \\ Q_{q\theta}(t) &= -\frac{1}{2}\rho_{air}V_\infty^2\int_0^{blade\ surface} x\,\varphi_\theta(y)\,Cp(x,y,t)\,dA \\ Q_\phi(t) &= -\frac{1}{2}\rho_{air}V_\infty^2\int_0^{blade\ surface} y\sin(\theta(y,t)+\beta)Cp(x,y,t)\,dA \end{aligned} \tag{28}$$

2.6.2 Flap forces

The same procedure applied for the blade forces is used for the flap surface with the addition of the flap DOF.

$$\delta \bar{W} = Q_{qh}\delta q_h + Q_{q\theta}\delta q_\theta + Q_\phi\delta\phi + Q_{flap}\delta q_{flap} = \int_0^{flap\ force} \vec{df}(x_e,y_e,t)\cdot\delta\vec{r}(x_e,y_e,t) \tag{29}$$

In this case the position vector is defined as:

$$\vec{r} = y\hat{r}_2 + h(y,t)\hat{r}_3 + (x+x_e)\hat{e}_1 + v(x_e,t)\hat{e}_3 \tag{30}$$

Therefore the generalized non-conservative forces over the flap are:

$$
\begin{aligned}
Q_{qh} &= \frac{1}{2}\rho_{air} V_\infty^2 \int_0^{flap\,surface} \varphi_h(y)\cos\theta(y,t) Cp(x_e, y_e, t)\, dA \\
Q_{q\theta} &= -\frac{1}{2}\rho_{air} V_\infty^2 \int_0^{flap\,surface} \varphi_\theta(y)(x + x_e) Cp(x_e, y_e, t)\, dA \\
Q_{\phi} &= -\frac{1}{2}\rho_{air} V_\infty^2 \int_0^{flap\,surface} y\sin(\theta(y,t)+\beta) Cp(x_e, y_e, t)\, dA \\
Q_{flap} &= \frac{1}{2}\rho_{air} V_\infty^2 \int_0^{flap\,surface} \left(\frac{x_e}{L_{xflap}}\right)^2 Cp(x_e, y_e, t)\, dA
\end{aligned}
\tag{31}
$$

2.7 Time nondimensionalization

In order to achieve regular aerodynamic vortex rings, the variables are nondimensionalized in time defining a nondimensional time variable t as follows:

$$
t = \frac{t^D}{TC}
$$

where:

$$
TC = \frac{LC}{VC}
\tag{32}
$$

VC is the reference free-stream velocity and LC is the chordwise length of a vortex ring in the bound lattice.

Replacing (32) into the time derivatives of (11) results in:

$$
\begin{pmatrix} h(t) \\ \theta(t) \\ \phi(t) \end{pmatrix}^D = \begin{pmatrix} LC\,h(t) \\ \theta(t) \\ \phi(t) \end{pmatrix} \rightarrow \begin{pmatrix} \dot{h} \\ \dot{\theta} \\ \dot{\phi} \end{pmatrix}^D = \frac{1}{TC}\begin{pmatrix} LC\,\dot{h} \\ \dot{\theta} \\ \dot{\phi} \end{pmatrix} \rightarrow \begin{pmatrix} \ddot{h} \\ \ddot{\theta} \\ \ddot{\phi} \end{pmatrix}^D = \frac{1}{TC^2}\begin{pmatrix} LC\,\ddot{h} \\ \ddot{\theta} \\ \ddot{\phi} \end{pmatrix}
\tag{33}
$$

where the D superscript defines dimensional.

2.8 Combining the models

Replacing (28), (31) and (33) into the blade equation of motion (11) and the flap static equilibrium equation (19), results in the complete equations of motion and flap equilibrium:

$$
\begin{bmatrix} \bar{m} & \bar{S}_y & \bar{S}_z \\ \bar{S}_y & \bar{I}_{yy} & \bar{I}_{\theta\phi} \\ \bar{S}_z & \bar{I}_{\theta\phi} & \bar{I}_{zz} \end{bmatrix}^D \begin{pmatrix} \ddot{q}_h \\ \ddot{q}_\theta \\ \ddot{\phi} \end{pmatrix} + TC^2 \begin{bmatrix} k_{hh} & 0 & 0 \\ 0 & k_{\theta\theta} & 0 \\ 0 & 0 & 0 \end{bmatrix}^D \begin{pmatrix} q_h \\ q_\theta \\ \phi \end{pmatrix} + \begin{bmatrix} 0 & \dot{q}_\theta b^D_{h\theta} & \dot{\phi} b^D_{h\phi} \\ 0 & 0 & \dot{\phi} b^D_{\theta\phi} \\ \dot{\phi} b^D_{\phi h} & \dot{q}_\theta b^D_{\phi\theta} & \dot{q}_\theta b^D_{\phi\phi} \end{bmatrix} \begin{pmatrix} \dot{q}_h \\ \dot{q}_\theta \\ \dot{\phi} \end{pmatrix} = \frac{1}{2}\rho_C LC^2 \begin{pmatrix} Q_{qh} \\ Q_{q\theta} \\ Q_\phi \end{pmatrix}
\tag{34}
$$

$$
q_{flap} = \frac{(Q_{flap} - F_{pzt})}{k_{flap}}
$$

2.9 Numerical integration

The numerical scheme follows the work of Preidikman et al (1999). The aeroelastic coupling is modeled in a staggered fashion as shown in figure 5. First the aerodynamic model is evolved to the next time step while keeping the structural mode frozen. Next, a new structural state is proposed with the updated aerodynamic loading. Then, the geometry is updated in the aerodynamic model while keeping the wake frozen. A correction is applied to the structural state and the error is evaluated. The scheme iterates until the error meets a tolerance criteria and then time advances again.

The predictor-corrector numerical scheme is the Hamming multistep method. This method requires the information of 4 previous states, so a starting procedure is required. The starting

procedure follows the same strategy exposed for the treatment of the fluid structure interaction. The difference is that the predictor-corrector scheme is changed as more states become available, therefore, the first step is solved with the improved Euler method and the rest are solved with Adams-Bashforth Adams-Moulton multistep methods.

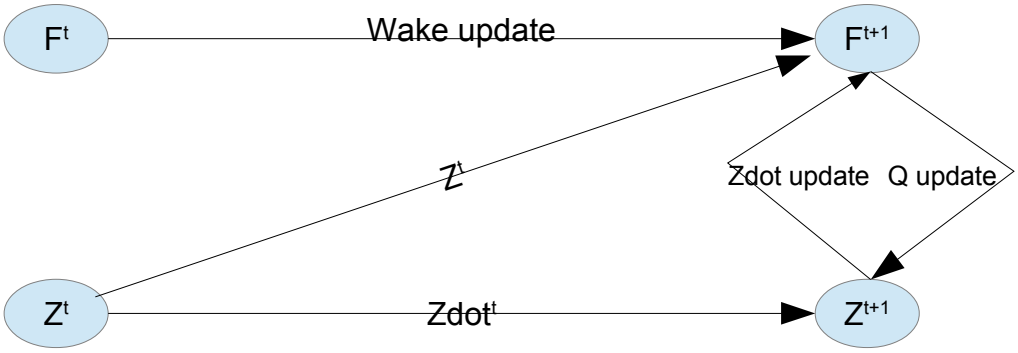

Figure 5: Fluid Structure Interaction scheme

3 ACTUATOR AND CONTROLLER DESIGN

3.1 Actuator

In order to study the actuator force and stiffness requirements, a baseline trailing edge flap was modeled with a bimorph piezoelectric architecture. The flap geometry was set as 1/6th of the local chord and the outer half of the surface span. The actuator stiffness and available force were scaled up from a reference actuator with known properties (see THUNDER datasheet). Two parameter sweep studies were performed to obtain the scaling parameters. The initial conditions for both tests were tip speed ratio (TSR) of 7 (maximum aerodynamic damping, Resor et al 2012) and no deflection and torsion angle. The objective for the geometry scaling was to achieve a maximum flap deflection of 15º at nominal operating conditions and zero input voltage (see Figure 6). A mechanical amplifying device was assumed to be embedded in the kinematic chain so as to produce the required force. The mechanical gain was defined so as to obtain a maximum flap deflection of 15º at nominal operating conditions and maximum input voltage (see Figure 7).

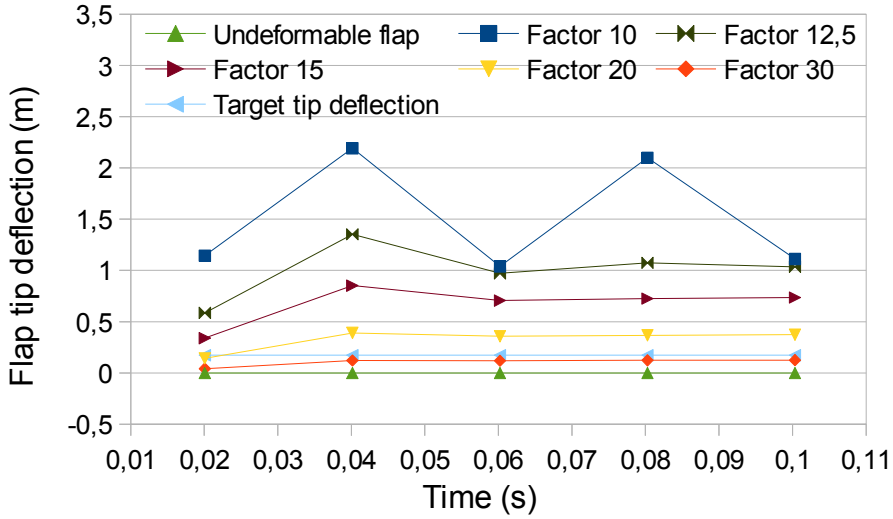

Figure 6: Geometrical scaling study results.

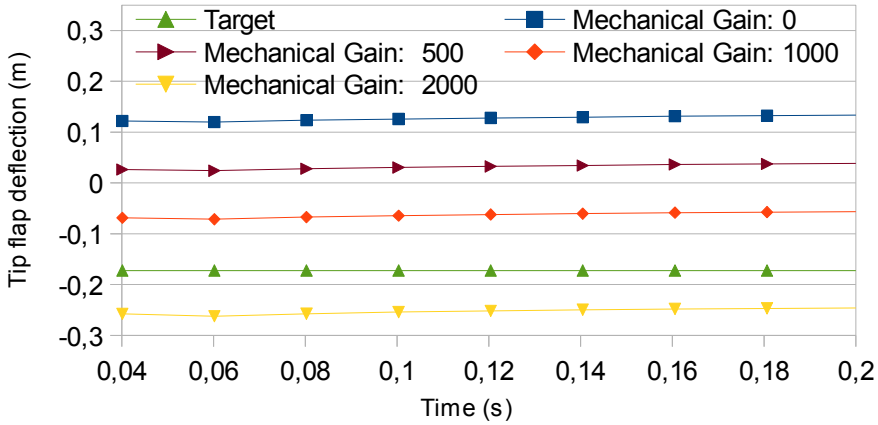

Figure 7: Force scaling study results.

3.2 Controller

The controller objective was to increase the torsional damping of the blade. For this purpose a simple derivative law was implemented. Since the flap deflection at the nominal tip speed ratio is not zero, a voltage offset is added to center the surface. The control law is:

$$u(t)=u_{offset}(TSR)+K_d\dot{q}_\theta(t) \tag{35}$$

where $u(t)$ is the control voltage, is the voltage required to center the flap (which is a function of the TSR) and K_d is the control gain.

To define the offset voltage a parameter sweep for different TSR was performed. In figure 8, the blue curve shows the voltage required for a null flap deflection for different TSR; while the yellow curve shows the proposed function for the controller.

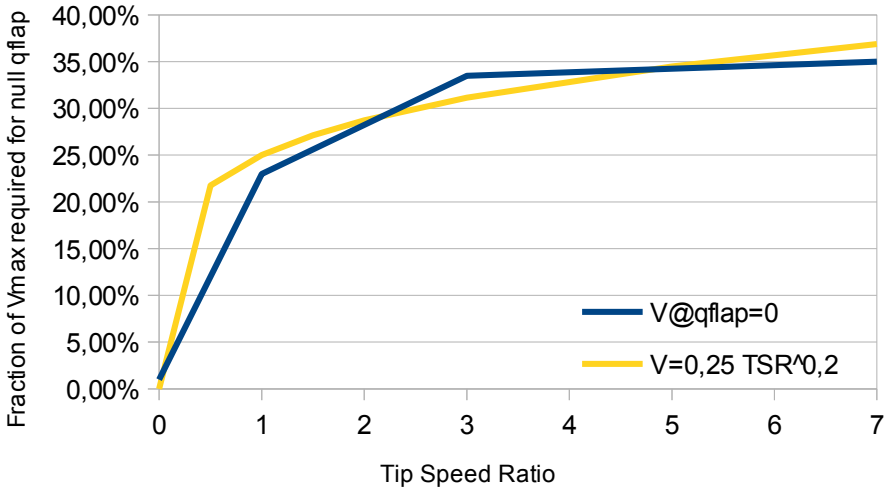

Figure 8: Offset voltage study results.

To define the control gain a final parameter sweep was performed. An initial estimate of the gain was calculated from the open-loop response of the surface. The torsional angle response results are shown in figure 9 for the initial estimate and a gain four times bigger.

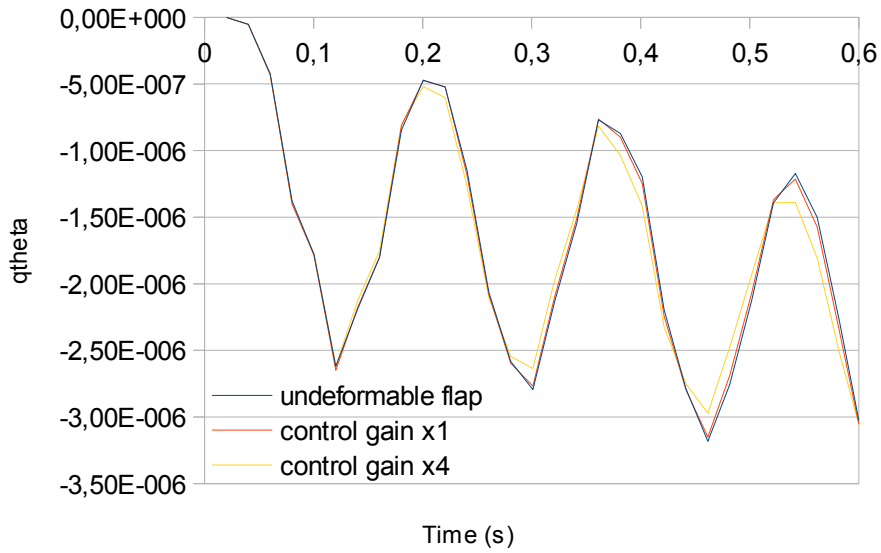

Figure 9: Control gain study results.

4 NUMERICAL EXPERIMENTS

4.1 Wind turbine blade

To demonstrate the effects of the rotating environment on the system behavior, numerical experiments were preformed on a wind turbine reference blade proposed by the National Renewable Energy Laboratory (NREL). The blade chord distribution and structural properties were taken from Griffith and Ashwill (2011). The blade surface is modeled as a flat surface with no twist and a variable chord. The blade elastic normal modes were extracted from the available data using a finite element code written by Bir G. (2012) and distributed by NREL. The modal shapes for an arbitrary set of points are shown in figures 10 and 11 along with the chosen approximating functions. For the bending mode there is a good agreement with a cubic function of the position y, but for the torsional one, a square function shows a closer agreement.

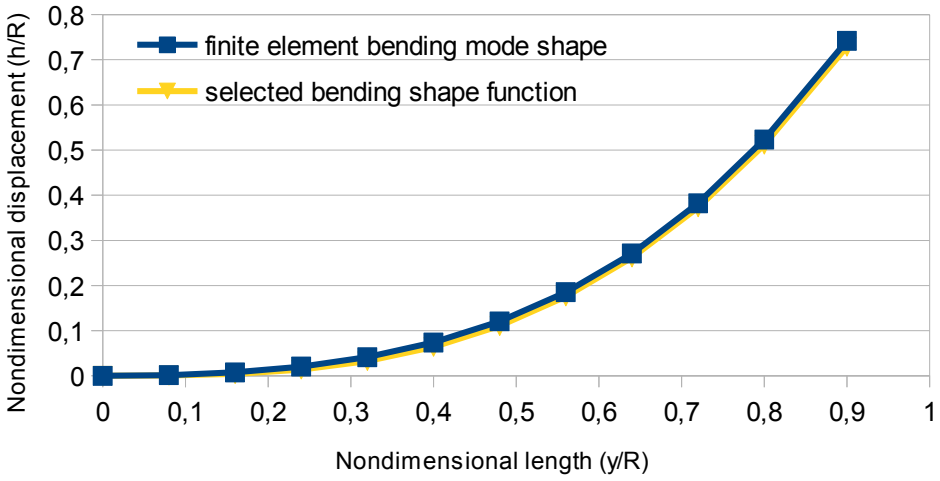

Figure 10: Bending mode.

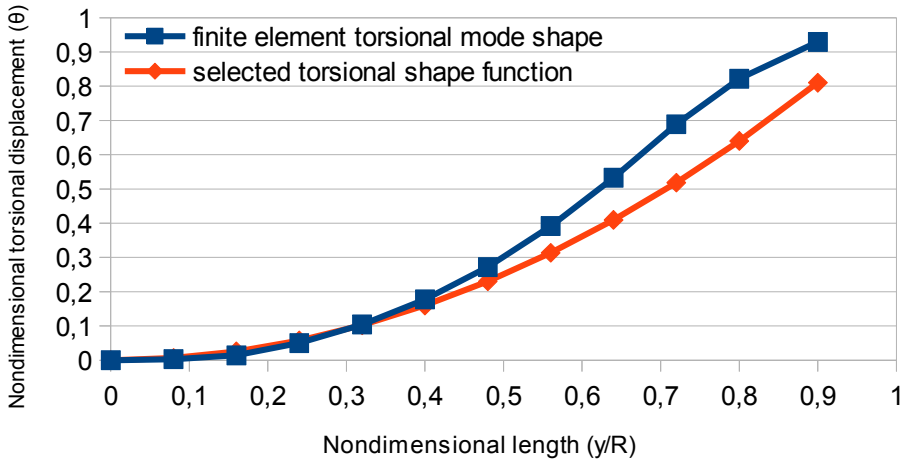

Figure 11: Torsional mode.

4.2 Test conditions:

The blade was meshed with 30 spanwise and 6 chordwise elements. The chosen time step for the integration of the coupled system was 0,02s. Four test cases were simulated at different initial TSR, in passive (no flap surface) and active (active flap surface) modes. In all test cases the air inflow was set at an angle of 90º relative to the blade surface and at a constant speed of 10m/s. The reference density was 1,225 kg/m^3. Since the blade chord distribution is not uniform along the span, the reference length was calculated from the mean aerodynamic chord (mac). In this case the calculated mac was 6,0205m ad the reference length1,0034m. Moreover, an initial, out of plane displacement of 1m was set in order to force a plunging motion for all cases.

4.3 Results

The results from the numerical experiments are presented in this section. Since the displacements are approximated by a single mode, the generalized coordinates vector temporal evolution is presented to describe the system response.
In figure 12 the temporal response of the torsional DOF is presented for the analyzed TSR. The red curves represent the cases were the flap has no deformation while the blue curves show the response due to the controlled flap activity. In all cases an important reduction in the vibration is achieved by means of the flap actuation.
In figure 13, the temporal evolution of the other DOF is shown for the TSR 7 case. The rotor movement seems undisturbed by the flap action, while the out-of-plane displacement shows a reduction in the vibration induced by the coupling of the torsional DOF.
Finally, in figure 14 a comparison of the critical damping ratio obtained for all test cases is plotted. Damping was measured from the logarithmic decay in the torsional DOF responses. There is a minor increase in the damping ratio due to the rotational motion for both the passive and active cases.

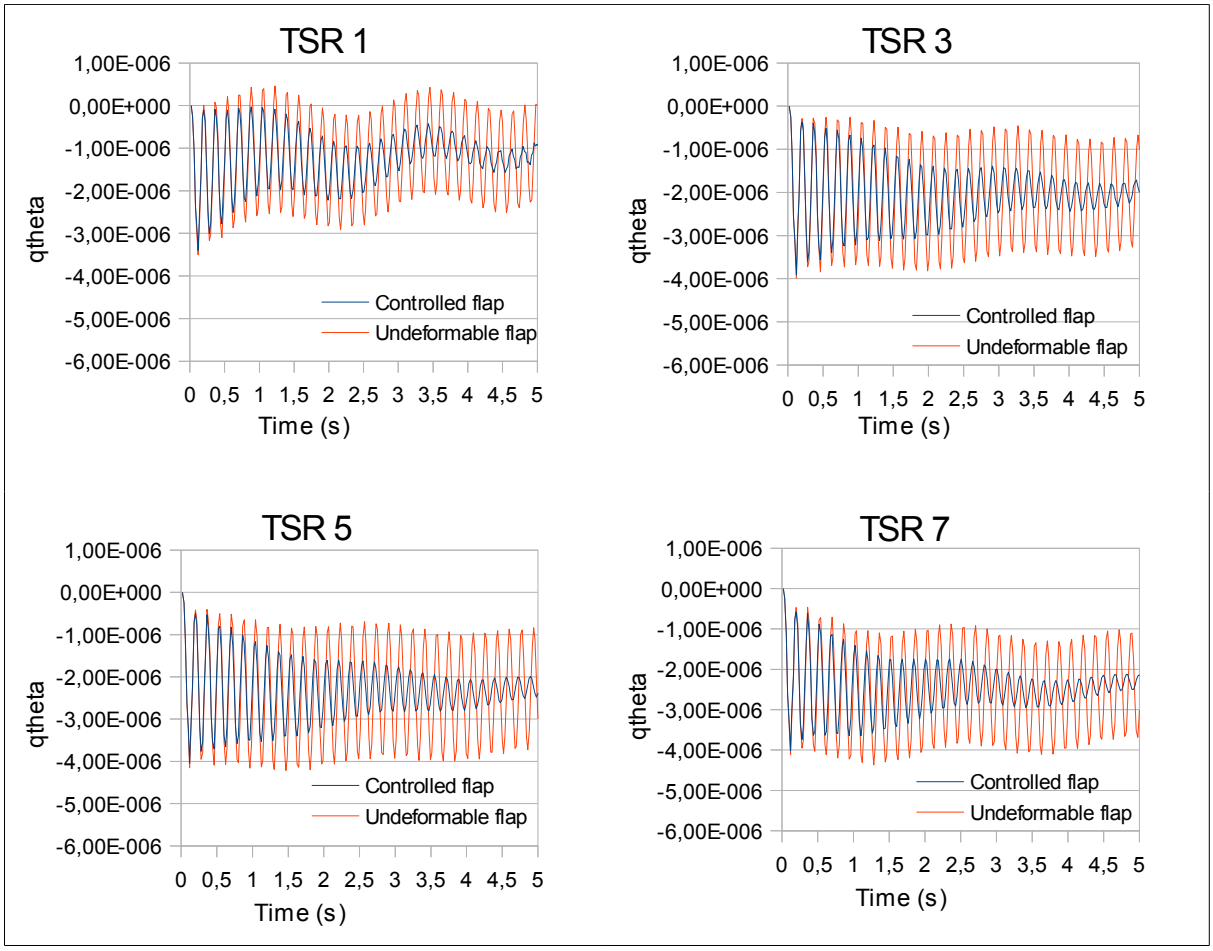

Figure 12: Torsional vibration results.

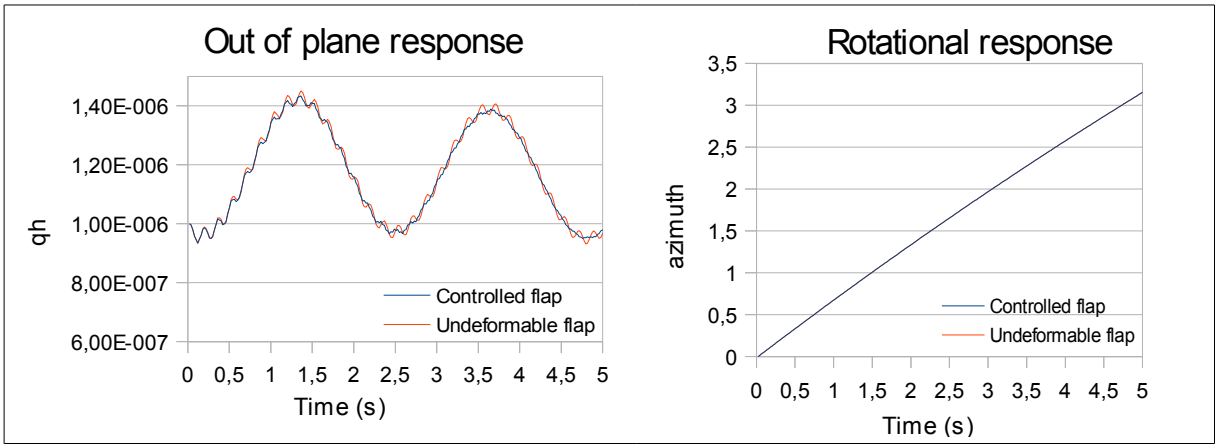

Figure 13: out of plane and rotational response for TSR 7.

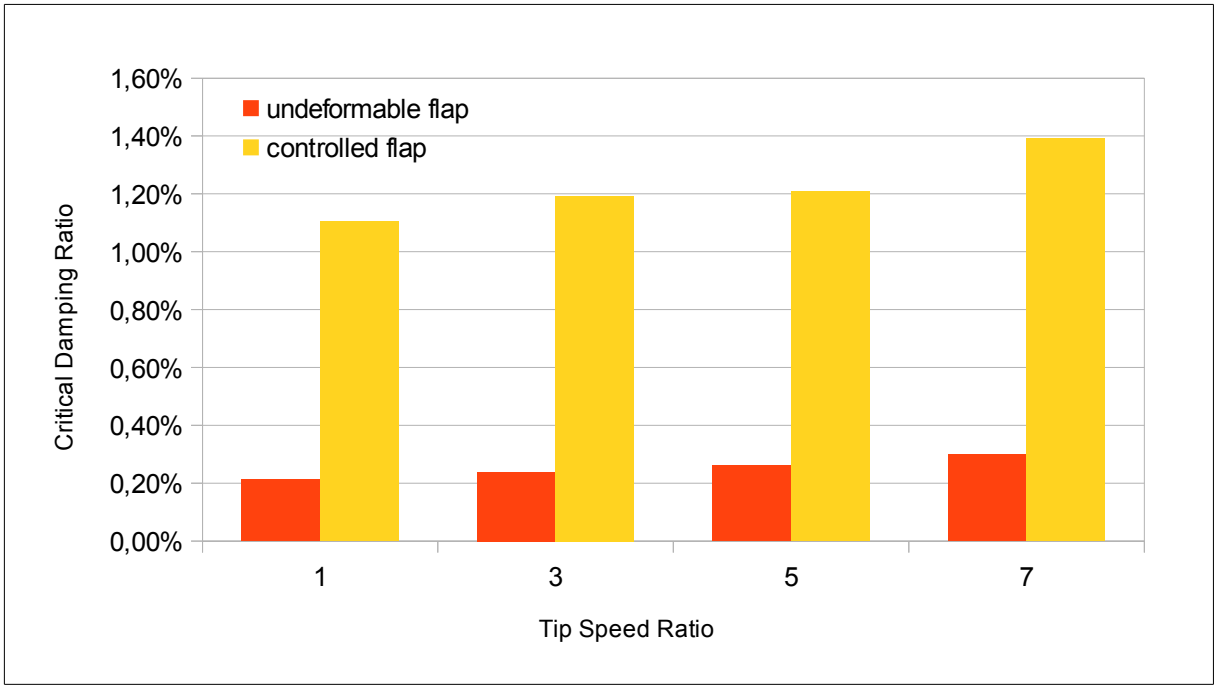

Figure 14: Critical damping results for different TSR and modes.

5 CONCLUSIONS

In the present paper, the analysis of the aeroservoelastic behavior of a lifting surface with a flexible piezoelectric actuator is extended to a non-inertial coordinate system that spins around an inertial one. The actuator is composed of a flexible trailing edge with embedded piezoelectric layers that enables the active control of the local aerodynamic forces. Structurally, both the flexible surface and flap are modeled as continuous beams with fixed-free end conditions. The displacements are described by a series expansion of assumed modes. The system aerodynamics are modeled with an unsteady version of the vortex lattice method. High Reynolds number flow is assumed, therefore viscous effects are confined at the boundary layers and the wake shed by the surface. Both surface and wake are idealized as vortex sheets which in turn are discretized with vortex rings. In order to capture the physical aspects from the fluid-structure-control interaction, the aerodynamic and structural numerical models are combined by means of a strong coupling technique. The system equations of motion are integrated iteratively in the time domain.

Numerical experiments were performed on a 100m blade proposed by the NREL fitted with a smart flexible flap. A derivative control law was implemented to set the input voltage for the piezoelectric actuator. The control parameters were tuned using parameter sweep studies on the blade-flap system. From the analysis of the actuator scaling parameters, it was found that the geometry needs be 30 times larger than the reference, which seems rather unfeasible. Also the piezoelectric force needs to be amplified by a factor of 2000 in order to best the aerodynamic loading and set the desired flap deformation.

Four test cases were simulated at different TSR, in passive (no flap surface) and active (deformable flap surface) modes. In all cases an important reduction in the vibration is achieved by means of the flap actuation. The rotor movement seems undisturbed by the flap action, while the out-of-plane displacement shows a reduction in the vibration induced by the coupling of the torsional DOF. The results show a minor increase in the damping ratio due to the rotational motion for both the passive and active cases.

REFERENCES

Barlas T. and Van Kuik G. Review of state of the art in smart rotor control research for wind turbines. *Progress in Aerospace Sciences*,46:1-27,2010.

Bir G. Bmodes. NREL, NWTC Design Codes, http://wind.nrel.gov/designcodes/preprocessors/bmodes, 2012

Buhl T., Bak D., Gaunaa M., Andersen P. Load alleviation through adaptive trailing edge control surfaces: ADAPWING overview. *EWEA Scientific proceedings*, 20-23,2007.

Face International Corporation, *THUNDER® TH-6R Data Sheet.* http://216.71.30.251/Face%20International/6r-ds.pdf

Felippa C., Park K., Farhat C. Partitioned analysis of coupled mechanical systems. *Computer Methods in Applied Mechanics and Engineering,* 190: 3247-3270, 2001.

Gebhardt C., Preidikman S., Massa J., Weber G., Comportamiento aerodinámico y aeroelástico de rotores de generadores eólicos de eje horizontal y de gran potencia. *Mecánica computacional*, 27:519-539, 2008.

Giurgiutiu V. Active-Materials Induced-Strain Actuation for Aeroelastic Vibration Control. *The Shock and Vibration Digest*¸ 32: 355-368, 2000.

Griffith T. and Ashwill T. The Sandia 100-meter All-glass Baseline Wind Turbine Blade: SNL100-00. Sandia National Laboratories. SAND2011-3779,2011

Jalili N. Piezoelectric-Based Vibration Control: From Macro to Micro/Nano Scale Systems. Springer, 2010.

Jonkman J. and Buhl M. FAST User's Guide. National Renewable Energy Laboratory, NREL/EL-500-29798, 2005.

Meirovitch L. Methods of Analytical Dynamics. McGrawHill, 1970.

Meirovitch L. Computational methods in structural dynamics. Sijthoff & Noordhoff, 1980.

Niezrecki C. et al. Piezoelectric Actuation: State of the Art. *The Shock and Vibration Digest,* 33: 269-280, 2001.

Pinkerton J. and Moses R. A Feasibility Study To Control Airfoil Shape Using THUNDER. *NASA*, TM-4767,1997

Preidikman S., Numerical Simulations of interactions among aerodynamics, structural dynamics and control systems. PhD thesis, Virginia Polytechnic Institute and State University, 1998.

Preidikman S.,Mook D., Time domain simulations of nonlinear, unsteady, aeroelastic behavior. *Mecánica computacional*, 19:361-370,1999.

Preidikman S., Massa J. and Bandi M. Accionamiento mediante actuadores piezoeléctricos de alas flexibles para micro-vehículos aéreos súper maniobrables inspirados en la biología. *Mecánica computacional*, 25:2359-2381,2006.

Resor, Owens, and Griffith. "Aeroelastic Instability of Very Large Wind Turbine Blades." Scientific Poster Paper; EWEA Annual Event, Copenhagen, Denmark, April 2012

Tripp N., Preidikman S., Mirasso A. Aeroservoelastic behavior of a wind turbine typical section with an active smart flexible flap. *Mecánica computacional*, 30:2233-2249,2011.